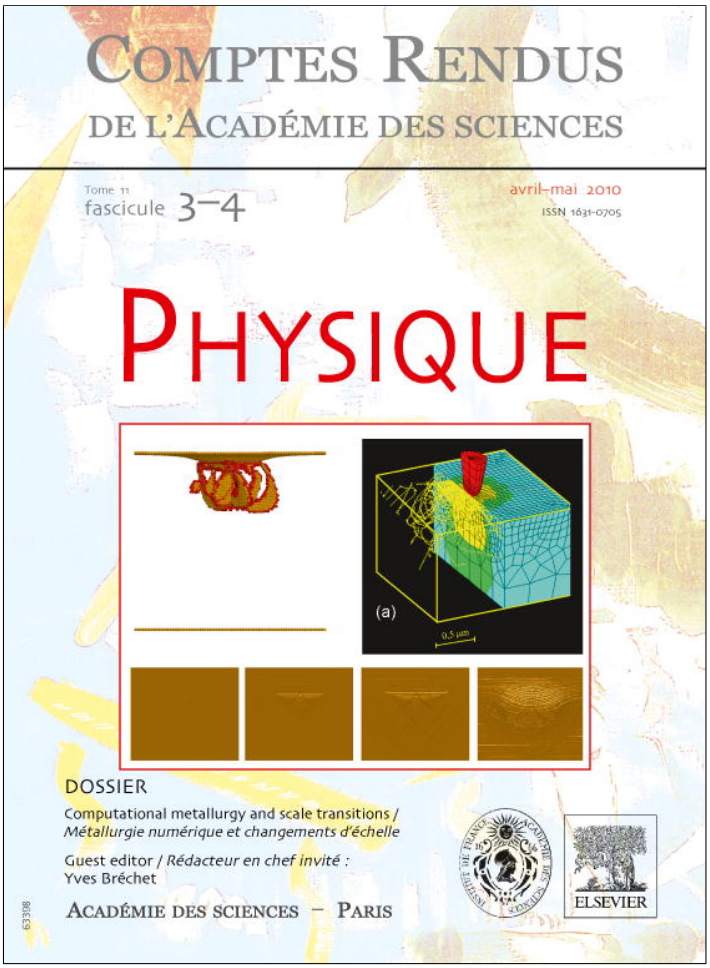

C. R. Physique 11 (2010) 293–303

Contents lists available at ScienceDirect

Comptes Rendus Physique

www.sciencedirect.com

Computational metallurgy and changes of scale / Métallurgie numérique et changements d'échelle

Finite element simulations of coherent diffraction in elastoplastic polycrystalline aggregates

Simulation par éléments finis de la diffraction cohérente dans des agrégats polycristallins élastoplastiques

H. Proudhon [a], N. Vaxelaire [b], S. Labat [b], S. Forest [a,*], O. Thomas [b]

[a] *MINES ParisTech, centre des matériaux, CNRS UMR 7633, BP 87, 91003 Evry cedex, France*
[b] *Aix-Marseille University, CNRS, IM2NP, FST, avenue Escadrille-Normandie–Niemen, 13397 Marseille cedex, France*

ARTICLE INFO

Article history:
Available online 16 August 2010

Keywords:
Coherent diffraction
Anisotropic elasticity
Crystal plasticity
Finite element modeling

Mots-clés :
Diffraction cohérente
Éasticité anisotrope
Plasticité cristalline
Modélisation par éléments finis

ABSTRACT

This work ties some crystal plasticity continuum mechanics computations with the diffraction theory. This allows one to predict coherent X-ray diffraction (CXD) patterns in reciprocal space in a polycrystalline specimen. When the sample deforms elastically, the full displacement field can be used to simulate CXD patterns, but it is no longer possible, as soon as plasticity develops within the considered grains. An approximate elastic displacement field, based on a first order Taylor expansion of the elastic deformation field near the center of the grain, is used to extend the predictions in the plastic regime. It is shown that using such a field leads to more realistic CXD patterns and therefore this approach could be useful to interpret coherent diffraction experiments in the future.

RÉSUMÉ

La théorie continue de la plasticité cristalline est utilisée pour prédire les figures de diffraction aux rayons X dans l'espace réciproque d'un polycristal métallique. Lorsque l'échantillon se déforme de manière purement élastique, le champ de déplacement calculé par éléments finis est utilisé pour simuler les figures de diffraction. Ce n'est plus possible dès que la plasticité se développe dans les grains étudiés. C'est la distorsion élastique qui intervient alors pour le calcul de diffraction. Un champ de déplacement approché, basé sur un développement de Taylor au premier ordre autour du centre d'un grain, est utilisé pour la prévision des figures de diffraction dans le régime plastique. On montre que l'usage de ce champ approché à la place du déplacement total conduit à des prévisions significativement différentes et plus réalistes des figures de diffraction. Cette approche peut donc être utile pour l'interprétation des expériences de diffraction cohérente.

* Corresponding author.
E-mail address: samuel.forest@ensmp.fr (S. Forest).

1631-0705/$ – see front matter
doi:10.1016/j.crhy.2010.07.009

1. Introduction

The deformation of metal polycrystals induces strong stress-strain heterogeneities at the grain level that are responsible for subsequent strain localisation at the macroscopic scale, intergranular/transgranular crack initiation, or decohesion in the case of thin films. Such heterogeneous strain fields can be estimated by means of continuum deformation models and simulations explicitly taking the grain morphology into account [1]. They are due to strain incompatibilities at grain boundaries resulting from elastic anisotropy, on the one hand, and from crystal plasticity on slip systems, on the other hand. Today, large scale simulations of elastoplastic polycrystalline aggregates can be performed thanks to the Finite Element method; more recently, the use of FFT based methods has been demonstrated [2].

The predicted mechanical fields can be compared to experimental full field measurements. Such comparisons are usually done at the free surface of deformed polycrystalline samples based on EBSD lattice orientation field measurements and grid deposition for measuring total strain fields [3]. The grain morphology below the surface then plays a significant role on the fields observed at the free surface, and specific attention must be paid to the modelling and characterisation of 3D grain shape, as shown in the case of elastic anisotropy in [4], and for crystal plasticity simulations in [5,6]. Experimental techniques giving access to the 3D grain morphologies and orientations or strain fields are best suited for comparisons between experiments and large scale computations of polycrystalline aggregates. Recent progress with X-ray diffraction and imaging techniques are very promising from this point of view [7]. The X-ray diffraction techniques can be used to determine lattice orientation fields and elastic strain fields and have already been successfully compared to simulations in a few cases [8,9].

More recently X-ray coherent diffraction has been recognised as a promising tool to experimentally characterise complex elastic strain fields in single crystals or grains in a polycrystal, up to very small length scales [10]. Such measurements can be performed on thin films, especially in polycrystalline films with columnar grains. The grain morphology in thin films can be efficiently handled by means of finite element simulations, taking elasticity and plasticity anisotropy effects into account [11,12].

The objective of the present work is to show how the available continuum crystal plasticity constitutive equations can be used to predict diffraction patterns and how large scale finite element simulations of polycrystalline films can help interpreting the evolution of experimental coherent diffraction patterns during straining. The case of anisotropic elastic behaviour is first considered to show how grain shape and strain heterogeneities inside grains affect the structure of diffraction patterns. When slip systems are activated in the grains, we propose to use available models of continuum crystal plasticity to estimate the impact of the elastic strain field on diffraction patterns. The proposed approach relies on the assumption that each material volume element contains enough dislocations for a continuum approach to hold. It would not apply to the analysis of strain fields around individual dislocations for which discrete dislocation methods combined with finite element simulations are better suited [13]. The proposed method is based on a clear distinction between elastic deformation (including stretching and rotation) of the lattice and plastic deformation that essentially leaves the crystal lattice unaffected within the continuum approximation.

The outline of the article is as follows. The coherent diffraction technique is first described in Section 2. The constitutive equations of continuum crystal elastoplasticity are recalled in Section 3, insisting on the transport rules for material and lattice directions. In the same section, we show how the information about total, elastic and plastic fields can be used to predict diffraction patterns. In the purely anisotropic elastic case, the full displacement field in some grains of the aggregates is used for post-processing diffraction patterns in Section 4 where the effect of grain shape and strain heterogeneities are analysed. In the elastoplastic case, the previous procedure must be amended since only the elastic deformation contributes to diffraction patterns. To illustrate this fact, we compare in Section 5 patterns obtained from the total displacement field to ones based on the information on the elastic deformation field only.

In the following, scalars, vectors, tensors of second and fourth rank are denoted by $a, \underline{\mathbf{a}}, \underset{\sim}{\mathbf{a}}, \underset{\approx}{\mathbf{a}}$, respectively.

2. Experimental X-ray coherent diffraction patterns

The goal of the experiment is to record the Bragg intensity from a single grain. Because of the low intensity of the diffracted signal a highly brilliant source such as the one delivered by the third generation synchrotron light sources, i.e. ESRF, Soleil, etc. is mandatory. The X-rays source is an undulator located at around 40 meters upstream the sample. The beam is monochromatized by a double Si $\langle 111 \rangle$ crystal. The number of windows along the beam is reduced to 1 to avoid coherence perturbations [14].

To measure the Bragg intensity from a single grain, a special design of the sample was made. A 10×10 µm^2 polycrystal was isolated in the center of a 150×150 µm^2 region where the initial gold thin film was etched by Focused Ion Beam. To be sure to find the region, the fluorescence signal of the gold was recorded thanks to a specific energy dispersive detector. To collect this fluorescence it is necessary to bring the energy above the L3 gold absorption edge which is excited for an energy up to 11.91 keV. The fluorescence map was very convenient to locate the region of interest.

The beam size on the sample is reduced using slits or Beryllium Lens which focus the X-ray beam on the sample. Thus only few grains are illuminated and thanks to the distribution of grain orientation, the grains do not diffract in the same direction. Then, it is easy to collect the scattered intensity from a single grain. The intensity measurements are achieved with a direct illuminated CCD camera from Andor with 1024×1024 pixels of 13×13 µm^2. The detector is positioned on a

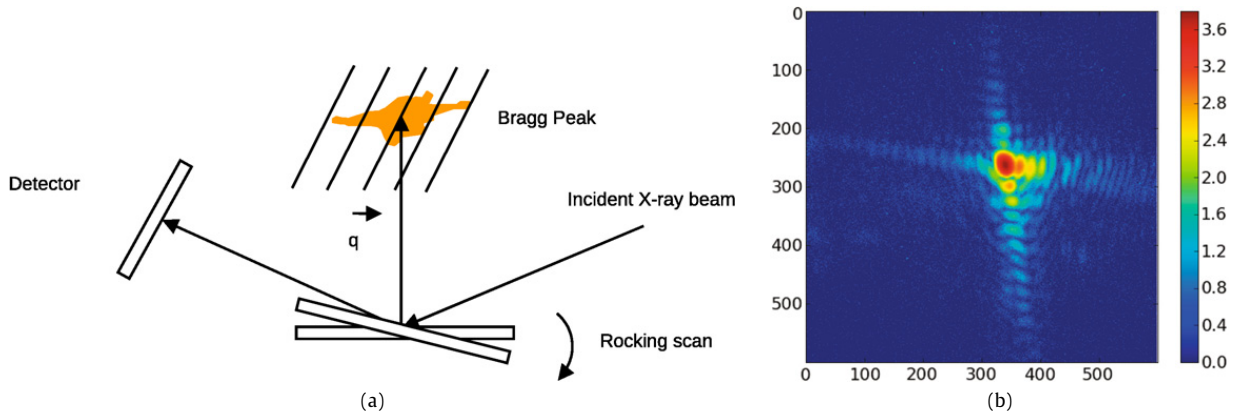

Fig. 1. 3D measurement of the Bragg peak: (a) schematic drawing of the experimental setup, (b) example of CXD pattern recorded under thermal loading.

Fig. 1. Mesure tridimensionnelle du pic de Bragg : (a) schéma du dispositif expérimental, (b) exemple de figure de diffraction cohérente enregistrée lors d'un chargement thermique.

2θ arm at around 1.2 meter from the sample to obtain a good angular resolution. A flight tube was used to limit absorption by air. The experimental noise was reduced by cooling down the CCD and by working in a single photon mode thanks to droplet algorithm [15]. This algorithm reduced the spreading of photon on the pixels and it is reasonable to neglect convolution pixel effect. The resolution δq in these working conditions reached in the plane of the CCD camera:

$$\delta q = \frac{1}{\lambda}\frac{S_{pixel}}{L} = 1.1 \times 10^{-4}\ \mathrm{nm}^{-1}$$

where λ is the X-ray wavelength, S_{pixel} the pixel size of the camera and L the distance between the sample and the camera.

A rocking scan is performed to obtain the 3D measurement of the Bragg peak (Fig. 1). Once the coherent diffraction pattern from a single grain inside the isolated polycrystal was recorded, a thermal cycle was performed. $\langle 111 \rangle$ Bragg reflection in a coplanar symmetric geometry was recorded. Each 2D slice of the reciprocal space corresponds to 200 measurements of 2 s. Typically the 3D acquisition yields a total count of 108 photons on the CCD with a maximum of around 7000 photons on one pixel. A uniform strain simply shifts the Bragg peak. On the other hand a distortion of the diffraction pattern is related to inhomogenous strains. In brief, the average strain in the grain is related to the global shift of the diffraction pattern whereas the distortion of the pattern is related to the strain variation within the grain.

Within the framework of the kinematic theory of diffraction,[1] the 3D intensity produced by a coherent beam diffracted by a small crystal is expressed as the sum of the complex amplitude scattered by each atom:

$$I(\underline{\mathbf{q}}) \propto \left| \sum_n f_n(\underline{\mathbf{q}}) \exp \imath \underline{\mathbf{q}}.\underline{\mathbf{X}}_n \right|^2 \tag{1}$$

with $\underline{\mathbf{X}}_n$ being the atomic position of atom n and f_n its scattering factor (constant for a pure metal like gold). The displacement field $\underline{\mathbf{u}}(\underline{\mathbf{X}})$ can be easily introduced and Eq. (1) can be rewritten using a Fourier transform:

$$I(\underline{\mathbf{q}}) \propto \left| TF\left\{ \rho(\underline{\mathbf{X}}). \exp\left(\imath \underline{\mathbf{G}}.\underline{\mathbf{u}}(\underline{\mathbf{X}})\right)\right\}\right|^2 \tag{2}$$

The diffracted intensity $I(\underline{\mathbf{q}})$ can therefore be evaluated using the displacement field computed by large scale finite element analysis of a polycrystal sample.

3. Continuum crystal plasticity framework

3.1. Constitutive equations

Continuum crystal plasticity is a special class of anisotropic elastoviscoplastic behaviour of materials. It relies on the precise knowledge of the kinematics of plastic slip according to crystallographic slip systems and of the driving force for activation of plastic slip, namely the corresponding resolved shear stress. When the number of dislocations inside the material volume element is high enough, a continuum description of plastic deformation and hardening can be formulated as settled in [16–18] and [19]. It is based on the multiplicative decomposition of the deformation gradient, $\underset{\sim}{\mathbf{F}}$, into an elastic part, $\underset{\sim}{\mathbf{E}}$, and a plastic part, $\underset{\sim}{\mathbf{P}}$:

$$\underset{\sim}{\mathbf{F}}(\underline{\mathbf{X}}) = \underset{\sim}{\mathbf{1}} + \frac{\partial \underline{\mathbf{u}}}{\partial \underline{\mathbf{X}}}, \qquad \underset{\sim}{\mathbf{F}}(\underline{\mathbf{X}}) = \underset{\sim}{\mathbf{E}}(\underline{\mathbf{X}}).\underset{\sim}{\mathbf{P}}(\underline{\mathbf{X}}) \tag{3}$$

[1] This assumption is valid because of the small reflected intensity compared to incident beam (large rocking curve ($\simeq 0.3°$)).

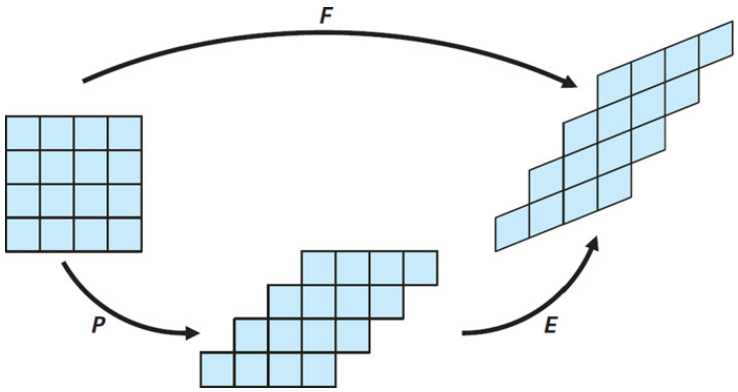

Fig. 2. Multiplicative decomposition of the deformation gradient into elastic and plastic parts.

Fig. 2. Décomposition multiplicative du gradient de la transformation en parties élastique et plastique.

The initial coordinates of the material point in the reference configuration are denoted by $\underline{\mathbf{X}}$. The current position of the material point in the current configuration is $\underline{\mathbf{x}}$. The displacement vector is $\underline{\mathbf{u}} = \underline{\mathbf{x}} - \underline{\mathbf{X}}$. The multiplicative decomposition (3) is associated with the definition of an intermediate configuration for which elastic strain is unloaded, see Fig. 2. The intermediate released configuration is uniquely determined up to a rigid body rotation which is chosen such that the lattice orientation in the intermediate configuration is the same as the initial one. Mandel calls it the isoclinic intermediate configuration. As a result, lattice rotation and distorsion during elastoplastic deformation are contained in the elastic deformation part $\underset{\sim}{\mathbf{E}}$, as examined at the end of this section.

In the case of elastoplastic deformation, the mass density of stress power takes the form:

$$J_e \underset{\sim}{\sigma} : \dot{\underset{\sim}{\mathbf{F}}}.\underset{\sim}{\mathbf{F}}^{-1} = \underset{\sim}{\mathbf{\Pi}}^e : \dot{\underset{\sim}{\mathbf{E}}}^e + \underset{\sim}{\mathbf{M}} : \dot{\underset{\sim}{\mathbf{P}}}.\underset{\sim}{\mathbf{P}}^{-1} \tag{4}$$

where $J_e = \det \underset{\sim}{\mathbf{E}}$ is the volume change from the intermediate to the current configuration, $\underset{\sim}{\mathbf{\Pi}}^e$ is the second Piola–Kirchhoff stress tensor with respect to the isoclinic intermediate configuration, $\underset{\sim}{\mathbf{E}}^e$ is the Green–Lagrange elastic strain measure and $\underset{\sim}{\mathbf{M}}$ is the Mandel stress tensor defined as:

$$\underset{\sim}{\mathbf{\Pi}}^e = J_e \underset{\sim}{\mathbf{E}}^{-1}.\underset{\sim}{\sigma}.\underset{\sim}{\mathbf{E}}^{-T}, \qquad \underset{\sim}{\mathbf{E}}^e = \frac{1}{2}\left(\underset{\sim}{\mathbf{E}}.\underset{\sim}{\mathbf{E}}^T - \underset{\sim}{\mathbf{1}}\right), \qquad \underset{\sim}{\mathbf{M}} = J_e \underset{\sim}{\mathbf{E}}^T.\underset{\sim}{\sigma}.\underset{\sim}{\mathbf{E}}^{-T} \tag{5}$$

Plastic deformation is the result of slip processes according to N slip systems characterised by the slip direction, $\underline{\mathbf{m}}^s$, and the normal to the slip plane, $\underline{\mathbf{n}}^s$, in the intermediate configuration:

$$\dot{\underset{\sim}{\mathbf{P}}}.\underset{\sim}{\mathbf{P}}^{-1} = \sum_{s=1}^{N} \dot{\gamma}^s \underline{\mathbf{m}}^s \otimes \underline{\mathbf{n}}^s \tag{6}$$

Constitutive equations for elastoviscoplastic materials are based on the definition of two potential functions, namely the free energy density function and the dissipation potential. The specific energy density, $\Psi(\underset{\sim}{\mathbf{E}}^e, T, \alpha)$, is a function of elastic strain, temperature and internal variables accounting for hardening properties. The corresponding state laws give the hyperelasticity relation and the entropy density, η:

$$\underset{\sim}{\mathbf{\Pi}}^e = \rho_i \frac{\partial \Psi}{\partial \underset{\sim}{\mathbf{E}}^e} = \underset{\approx}{\mathbf{C}} : \underset{\sim}{\mathbf{E}}^e, \qquad \eta = -\frac{\partial \Psi}{\partial T} \tag{7}$$

where a quadratic potential for elasticity has been proposed, thus introducing the fourth rank tensor of elasticity moduli, $\underset{\approx}{\mathbf{C}}$. Such an assumption is realistic for metals since elastic strain usually remains small, as discussed in the next subsection. The mass density of the material point with respect to the intermediate configuration is denoted by ρ_i. The dissipation rate associated with slip processes takes the form, in the isothermal case,

$$\underset{\sim}{\mathbf{M}} : \dot{\underset{\sim}{\mathbf{P}}}.\underset{\sim}{\mathbf{P}}^{-1} + X\dot{\alpha} = \sum_{s=1}^{N} \tau^s \dot{\gamma}^s + X\dot{\alpha} \geqslant 0 \tag{8}$$

where $X = -\rho_i \partial \Psi / \partial \alpha$ are the thermodynamic forces associated with the internal variables α. The resolved shear stress $\tau^s = \underline{\mathbf{m}}^s.\underset{\sim}{\mathbf{M}}.\underline{\mathbf{n}}^s$ on slip system s is the driving force for activation of slip. The first term in the previous inequality is the plastic power whereas the second term accounts for energy storage associated with hardening. Positivity of dissipation rate is ensured if there exists a convex dissipation potential $\Omega(\underset{\sim}{\mathbf{M}}, X)$ from which the plastic flow and hardening rules are derived:

$$\dot{\underset{\sim}{\mathbf{P}}}.\underset{\sim}{\mathbf{P}}^{-1} = \frac{\partial \Omega}{\partial \underset{\sim}{\mathbf{M}}}, \qquad \dot{\alpha} = \frac{\partial \Omega}{\partial X} \tag{9}$$

The full continuum thermodynamics framework for the formulation of non-linear constitutive equations for crystalline solids can be found in [20]. Specific hardening laws including evolution equations for dislocation densities can be found for example in [21]. In the present contribution, examples will be given in the case of perfect placticity, i.e. without hardening so that we will not consider α variables. The flow rule (9) used in the present work is specified for single crystals for which the dissipation potential can be regarded as a function of the N resolved shear stresses τ^s:

$$\dot{\gamma}^s = \frac{\partial \Omega}{\partial \tau^s} = \left\langle \frac{|\tau^s| - \tau_c}{K} \right\rangle^n \operatorname{sign}(\tau^s), \qquad \Omega(\tau^s) = \sum_{s=1}^{N} \frac{K}{n+1} \left\langle \frac{|\tau^s| - \tau_c}{K} \right\rangle^{n+1} \tag{10}$$

where τ_c is the critical resolved shear stress for the considered family of slip systems, for example the 12 octahedral slip systems in fcc crystals. The brackets $\langle x \rangle$ denote the positive part of x. As a result, no plastic slip occurs as long as

$$\left|\tau^s\right| < \tau_c^s \tag{11}$$

in accordance with Schmid's law for single crystals. Viscosity parameters are K and n in (10). They can be chosen such that plastic processes are almost rate-independent in a given range of applied strain rates.

3.2. Prediction of coherent diffraction patterns

The previous continuum mechanical approach makes it possible to distinguish between the transformation of material and lattice directions. Material lines are made of material points that are subjected to the motion $\underline{\mathbf{u}}(\underline{\mathbf{X}})$. The tangent to a material line at $\underline{\mathbf{X}}$ is a material direction $\underline{\mathbf{d}}$ in the reference configuration that transforms into the material direction $\underline{\mathbf{d}}'$ in the current configuration by means of the deformation gradient:

$$\underline{\mathbf{d}}'(\underline{\mathbf{X}}) = \underset{\sim}{\mathbf{F}}(\underline{\mathbf{X}}).\underline{\mathbf{d}}(\underline{\mathbf{X}}) \tag{12}$$

In contrast, lattice directions are not material insofar as they are not necessarily made of the same material points (atoms) in the initial and current configurations due to the passing of dislocations, but keep the same crystallographic meaning. According to the concept of isoclinic configuration, lattice directions are unchanged from the initial to the intermediate configuration of Fig. 2. Glide of dislocations through, and thus leaving, the material volume element does not distort nor rotate the lattice, although material lines are sheared. According to the continuum theory of dislocations, statistically stored dislocations accumulating in the material volume element affect material hardening but do not change the element shape. Accordingly, an initial lattice direction $\underline{\mathbf{d}}^\sharp$ is transformed into $\underline{\mathbf{d}}^{\sharp\prime}$ by means of the elastic deformation:

$$\underline{\mathbf{d}}^{\sharp\prime}(\underline{\mathbf{X}}) = \underset{\sim}{\mathbf{E}}(\underline{\mathbf{X}}).\underline{\mathbf{d}}^\sharp(\underline{\mathbf{X}}) \tag{13}$$

The previous transport rules have the following consequences for the prediction of diffraction patterns based on the continuum elastoplasticity theory:

- *No plastic deformation.* In the absence of plastic deformation, we have $\underset{\sim}{\mathbf{P}} = \underset{\sim}{\mathbf{1}}$ and the deformation gradient coincides with the elastic deformation, $\underset{\sim}{\mathbf{F}} = \underset{\sim}{\mathbf{E}}$. In that case, the intensity of diffracted beam is given by formula (2) where $\underline{\mathbf{u}}$ is the material displacement field from which the deformation gradient $\underset{\sim}{\mathbf{F}}$ derives.
- *Homogeneous elastoplastic deformation.* In that case, the displacement field $\underline{\mathbf{u}}(\underline{\mathbf{X}})$ is not the relevant quantity any more to compute the diffracted intensity. According to (13), only the elastic deformation affects lattice directions. For a homogeneous transformation, meaning that $\underset{\sim}{\mathbf{F}}$, $\underset{\sim}{\mathbf{E}}$ and $\underset{\sim}{\mathbf{P}}$ do not depend on $\underline{\mathbf{X}}$, an elastic displacement field can be defined as

  $$\underline{\mathbf{u}}^e(\underline{\mathbf{X}}) = (\underset{\sim}{\mathbf{E}} - \underset{\sim}{\mathbf{1}}).(\underline{\mathbf{X}} - \underline{\mathbf{X}}_0) \tag{14}$$

  up to an arbitrary translation embodied by the choice of the origin $\underline{\mathbf{X}}_0$, which does not affect the diffraction pattern. The diffraction intensity can then be computed as

  $$I(\underline{\mathbf{q}}) \propto \left| TF\left\{ \rho(\underline{\mathbf{X}}). \exp\left(\imath \underline{\mathbf{G}}.\underline{\mathbf{u}}^e(\underline{\mathbf{X}})\right)\right\}\right|^2 \tag{15}$$

- *Non-homogeneous elastoplastic deformation.* In that case, the elastic deformation field $\underset{\sim}{\mathbf{E}}(\underline{\mathbf{X}})$ is generally not a compatible field, meaning that there exists no vector field $\underline{\mathbf{u}}^e(\underline{\mathbf{X}})$ of which $\underset{\sim}{\mathbf{E}}(\underline{\mathbf{X}})$ is the gradient. Different approximations can be proposed to estimate the diffraction pattern resulting from non-homogeneous elastoplastic deformation. We can start from a Taylor expansion for a given material point $\underline{\mathbf{X}}_0$, for instance, the center of a grain as done in Section 5:

  $$\underline{\mathbf{u}}^e_{approx}(\underline{\mathbf{X}}) = \left(\underset{\sim}{\mathbf{E}}(\underline{\mathbf{X}}_0) - \underset{\sim}{\mathbf{1}}\right).(\underline{\mathbf{X}} - \underline{\mathbf{X}}_0) + \frac{1}{2}\frac{\partial \underset{\sim}{\mathbf{E}}}{\partial \underline{\mathbf{X}}}(\underline{\mathbf{X}}_0) : (\underline{\mathbf{X}} - \underline{\mathbf{X}}_0) \otimes (\underline{\mathbf{X}} - \underline{\mathbf{X}}_0) + \cdots \tag{16}$$

A truncated Taylor expansion can be inserted in Eq. (15). It requires the evaluation of elastic deformation field and its higher order gradients. We propose here an alternative estimation obtained by replacing $\underset{\sim}{\mathbf{E}}(\underline{\mathbf{X}}_0)$ by $\underset{\sim}{\mathbf{E}}(\underline{\mathbf{X}})$ in the first term of the previous Taylor expansion:

$$\underline{\mathbf{u}}^e_{approx}(\underline{\mathbf{X}}) = \big(\underset{\sim}{\mathbf{E}}(\underline{\mathbf{X}}) - \underset{\sim}{\mathbf{1}}\big).(\underline{\mathbf{X}} - \underline{\mathbf{X}}_0) \tag{17}$$

Such a heuristic approximation has proved to be an efficient estimate in a different context of multiscale asymptotic expansion in [22]. It requires the post-processing of the elastic deformation field, which is readily available from the results of Finite Element analyses. The formula (17) will be used in Section 5 in order to evidence the deviation of the obtained diffraction patterns from the one computed from the total displacement field $\underline{\mathbf{u}}(\underline{\mathbf{X}})$.

The exploitation of diffraction patterns is confined to limited strain levels so that a real correlation can be found between the initial and final patterns. The kinematics of elastoplastic deformation recalled in Section 3.1 can be expanded in the case of small strains and small rotations, based on the polar decompositions of total, elastic and plastic deformation:

$$\underset{\sim}{\mathbf{E}} = \underset{\sim}{\mathbf{R}}^e.\underset{\sim}{\mathbf{U}}^e \simeq \big(\underset{\sim}{\mathbf{1}} + \underset{\sim}{\omega}^e\big).\big(\underset{\sim}{\mathbf{1}} + \underset{\sim}{\varepsilon}^e\big) \simeq \underset{\sim}{\mathbf{1}} + \underset{\sim}{\varepsilon}^e + \underset{\sim}{\omega}^e \tag{18}$$

$$\underset{\sim}{\mathbf{P}} = \underset{\sim}{\mathbf{R}}^p.\underset{\sim}{\mathbf{U}}^p \simeq \big(\underset{\sim}{\mathbf{1}} + \underset{\sim}{\omega}^p\big).\big(\underset{\sim}{\mathbf{1}} + \underset{\sim}{\varepsilon}^p\big) \simeq \underset{\sim}{\mathbf{1}} + \underset{\sim}{\varepsilon}^p + \underset{\sim}{\omega}^p \tag{19}$$

where $\underset{\sim}{\mathbf{R}}^e$, $\underset{\sim}{\mathbf{R}}^p$ and $\underset{\sim}{\mathbf{U}}^e$, $\underset{\sim}{\mathbf{U}}^p$ are rotations and symmetric stretch tensors, respectively. Accordingly, $\underset{\sim}{\varepsilon}^e$, $\underset{\sim}{\omega}^e$ (resp. $\underset{\sim}{\varepsilon}^p$, $\underset{\sim}{\omega}^p$) represent small elastic (resp. plastic) strain and rotation. The elastic rotation accounts for lattice rotation, as follows from the proposed kinematics of plastic slip. Similarly, the following holds for the total deformation:

$$\underset{\sim}{\mathbf{F}} = \underset{\sim}{\mathbf{R}}.\underset{\sim}{\mathbf{U}} = (\underset{\sim}{\mathbf{1}} + \underset{\sim}{\omega}).(\underset{\sim}{\mathbf{1}} + \underset{\sim}{\varepsilon}) \simeq \underset{\sim}{\mathbf{1}} + \underset{\sim}{\varepsilon} + \underset{\sim}{\omega} \tag{20}$$

so that

$$\underset{\sim}{\varepsilon} = \underset{\sim}{\varepsilon}^e + \underset{\sim}{\varepsilon}^p, \qquad \underset{\sim}{\omega} = \underset{\sim}{\omega}^e + \underset{\sim}{\omega}^p \tag{21}$$

where all strain tensors are symmetric whereas all ω tensors are skew-symmetric. As a result, in the context of small strains and rotations, the formula (17) can be replaced by:

$$\underline{\mathbf{u}}^e_{approx}(\underline{\mathbf{X}}) = \big(\underset{\sim}{\varepsilon}^e(\underline{\mathbf{X}}) + \underset{\sim}{\omega}^e(\underline{\mathbf{X}})\big).(\underline{\mathbf{X}} - \underline{\mathbf{X}}_0) \tag{22}$$

4. Grain shape and strain heterogeneity effect on coherent diffraction patterns

In this part elastic computations have been carried out using the FE software package Z-Set/ZeBuLoN[2] using a synthetic polycrystalline microstructure created from a 2D Voronoi tessellation. The 2D grain morphology was extended in the third direction to produce a 3D model with a size of $500 \times 500 \times 50$ µm^3 (cf. Fig. 3). This simplified procedure can well represent the real microstructure of columnar grains in thin films and has been recently used to simulate the strain heterogeneities within copper thin films [12]. Grain orientations have been set according to a fibre texture ($\langle 111\rangle$ axis normal to the film surface) with random in-plane orientation. A single grain received a $\langle 100\rangle$ orientation to study the effect of neighboring grains with different orientations. The diffraction pattern is computed for two different grains (numbers #06 and #39) respectively oriented $\langle 111\rangle$ and $\langle 100\rangle$ (see Fig. 3). Those grains are located close to the center to avoid any boundary effect.

More precisely, having carried out the mechanical calculation, the 3D diffraction pattern is computed from the displacement field with a fast Fourier transform using Eq. (2). This involves a complex 3D FFT of the field $\underline{\mathbf{u}}(\underline{\mathbf{X}})$ which needs to be transferred on a regular grid. To avoid any possible affect due to the field transfer, the regular mesh is finer than all the meshes used in this work (see Section 4.1).

The present FE computations use a linear elastic behaviour with cubic anisotropy to represent the gold crystal. The following elastic constants C_{ij} have been used [23]: $C_{11} = 192\,340$ MPa, $C_{12} = 163\,140$ MPa and $C_{44} = 41\,950$ MPa. For fcc crystals, the Bragg vector is $\underline{\mathbf{G}}_{hkl} = \frac{2\pi}{a}[h,k,l]$ with a the atomic spacing taken to be $a = 0.4078$ nm. The effect of temperature on these parameters is neglected.

4.1. Influence of mesh density

It is well known that convergence of stress and strain fields predicted by FE is reached only if sufficiently small element size is used. To study the effect of mesh refinement on the shape of predicted CXD patterns, several meshes of the same microstructure (m_5, m_3, m_2, m_1 from coarser to finer) have been created (see Table 1). The same regular grid of $100 \times 100 \times 10$ elements is used to transfer the displacement field. The evolution of the $\langle 111\rangle$ Bragg peak simulated for grain #39 with an average strain of 1% can be seen in Fig. 4. Subtle modifications appear as the mesh is refined more and more but those tend to rapidly decrease. Results using mesh m_2 are considered to be satisfactory.

[2] http://www.nwnumerics.com.

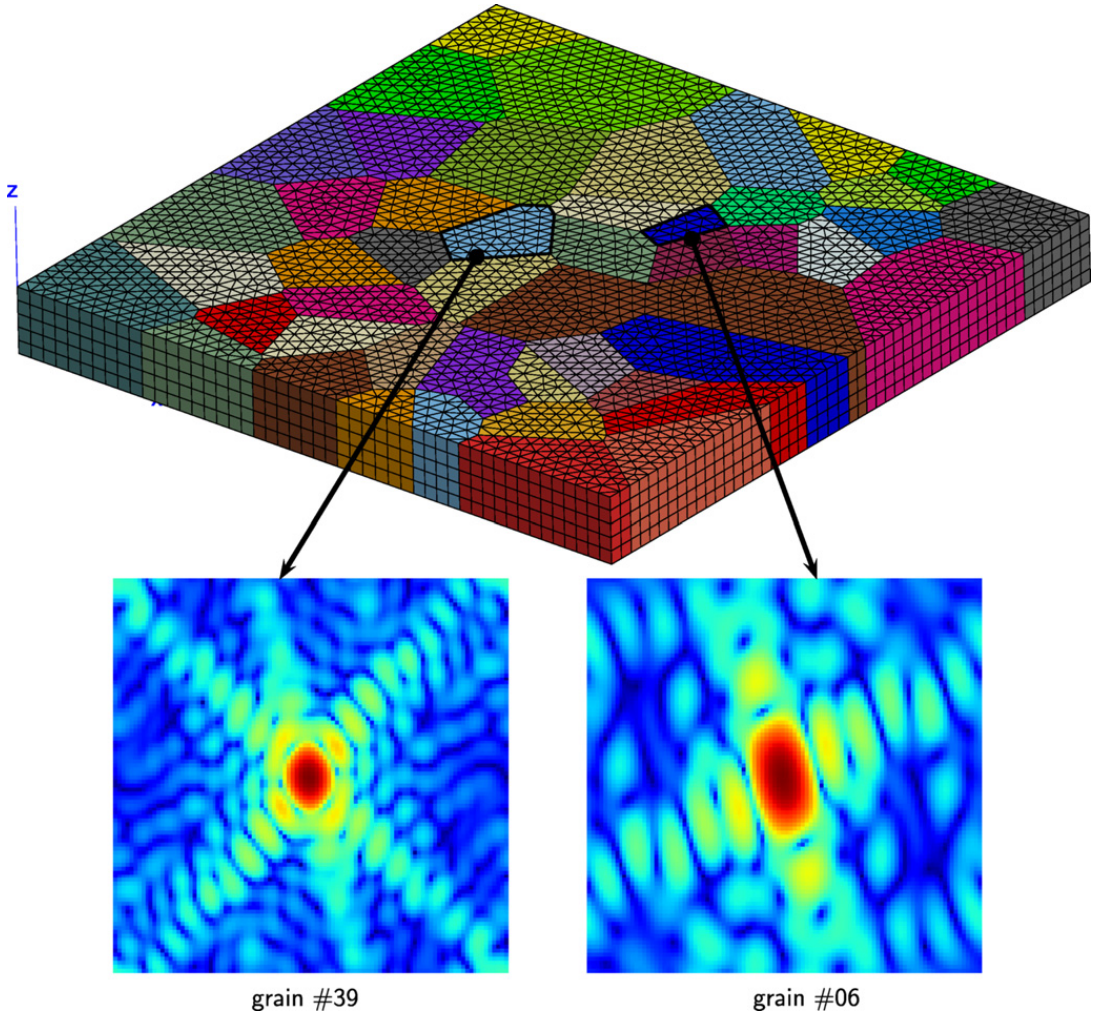

Fig. 3. Synthetic polycrystalline microstructure used to evaluate grain shape and strain heterogeneity effect on coherent diffraction patterns; two grains are highlighted and the corresponding diffraction patterns before any deformation is applied are shown (the pattern is here a signature of the grain shape since the crystals are undeformed).

Fig. 3. Microstructure polycristalline synthétique utilisée pour évaluer l'effet de forme de grain et d'hétérogénéité de déformation sur les figures de diffraction cohérente ; deux grains sont soulignés et les figures de diffraction correspondantes avant déformation sont illustrées.

Table 1
Details of the mesh refinement.

Tableau 1
Finesse des maillages par éléments finis utilisés.

Mesh	m_5	m_3	m_2	m_1
Total number of elements	1172	5940	27 430	224 410
Elements in grain 06	32	93	460	3860
Elements in grain 39	12	45	160	1340

4.2. Effect of the strain level

The sample is loaded under tension applying a lateral displacement corresponding to a global axial strain of 1%. Calculation results are presented together with the evolution of the diffraction patterns in both grains in Fig. 5.

During straining, the Bragg peaks undergo at the same time a shift in the reciprocal space and a change of shape. The shift can be related to the average gradient of the displacement field within the grain (a constant value of displacement corresponding to a translation would not affect it) and shape distortions are directly related to the deformation field heterogeneities. One can note that the strain effect is more pronounced for the grain oriented ⟨100⟩ than for the grain oriented ⟨111⟩ (one can see a series of fringes disappear). This is a signature of the stronger strain heterogeneities in this grain due to the higher crystalline misorientation with the neighboring grains. In addition, the shape evolution of the CXD pattern seems to be in qualitative agreement with experimental measurements as seen for instance in [10].

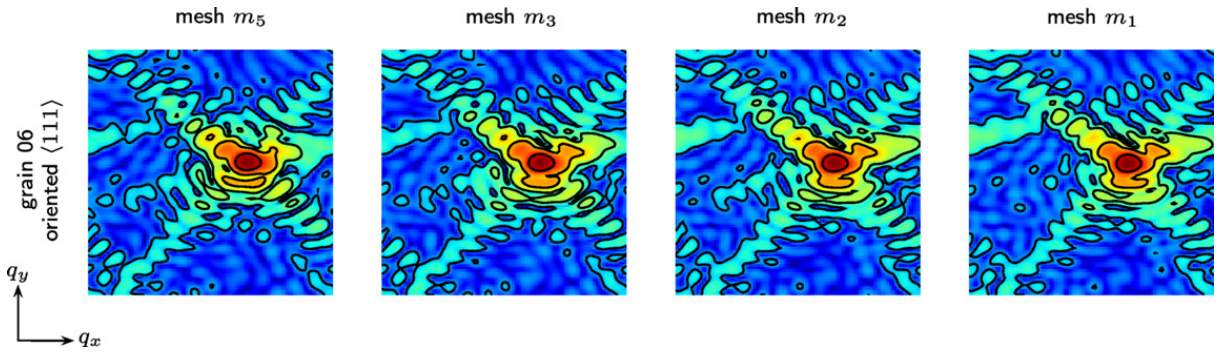

Fig. 4. CXD pattern computed for reflection ⟨111⟩ of grain #39 with an average elastic strain of 1%; the diffraction pattern changes slightly when the mesh is refined (the picture uses a normalised log scale, contours highlight levels 0.3, 0.5, 0.7, 0.9).

Fig. 4. Figures de diffraction cohérente calculées pour la réflexion des plans ⟨111⟩ du grain #39 avec une déformation élastique moyenne de 1% ; la figure de diffraction change légèrement lorsque le maillage est raffiné (une échelle log normalisée est utilisée pour la figure, les isovaleurs indiquent les niveaux 0,3, 0,5, 0,7, 0,9).

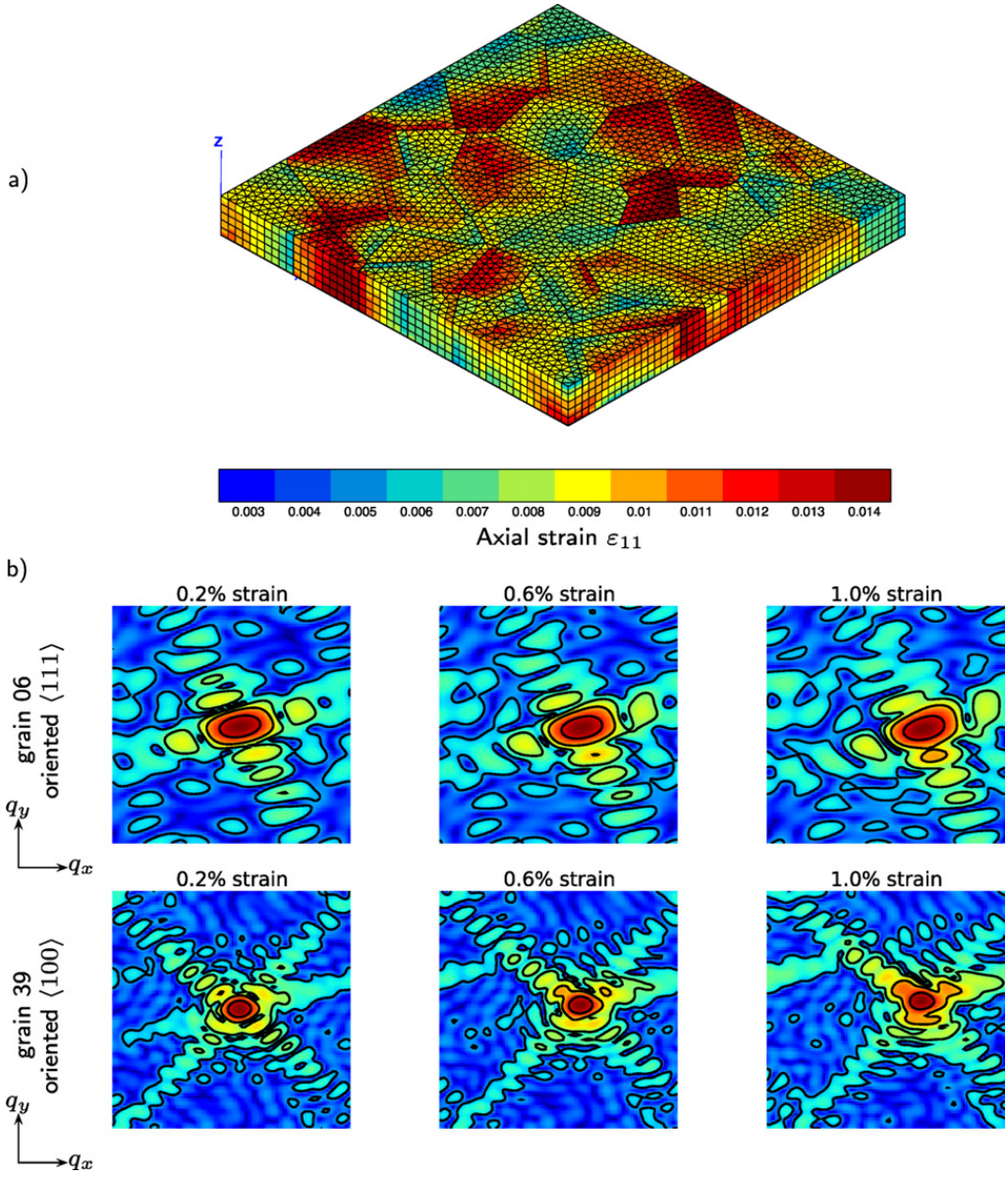

Fig. 5. (a) Field of axial strain component ε_{11} in the deformed polycrystal, both studied grain are highlighted, (b) evolution of the Bragg peak ⟨111⟩ during the mechanical loading (normalised log scale, contours highlight levels 0.3, 0.5, 0.7, 0.9).

Fig. 5. (a) Champ de déformation axiale ε_{11} dans le polycristal déformé, (b) evolution du pic de Bragg ⟨111⟩ pendant la déformation mécanique (une échelle log normalisée est utilisée pour la figure, les isovaleurs indiquent les niveaux 0,3, 0,5, 0,7, 0,9).

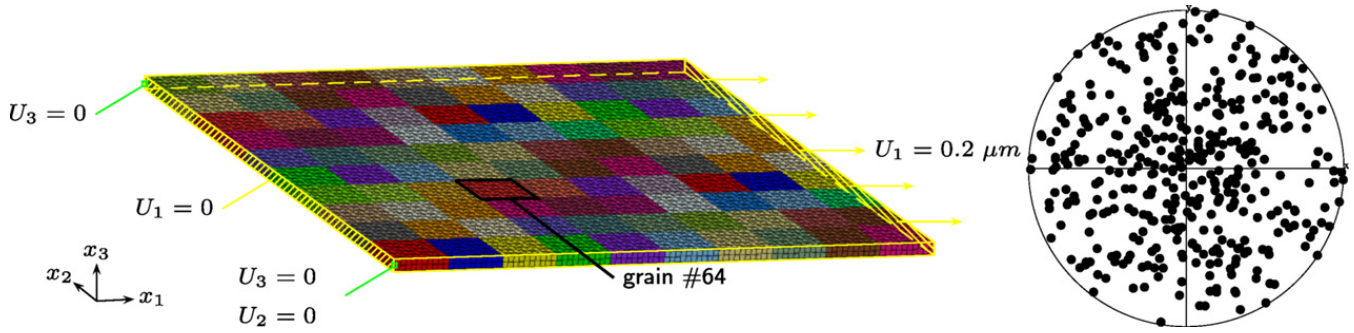

Fig. 6. Polycrystalline sample with square grains using random grain orientations (⟨111⟩ pole figure is shown) used for elastoplastic computations.

Fig. 6. Echantillon polycristallin à grains carrés avec des orientations aléatoires (la figure de pôles ⟨111⟩ est indiquée) utilisé pour les calculs en élastoplasticité.

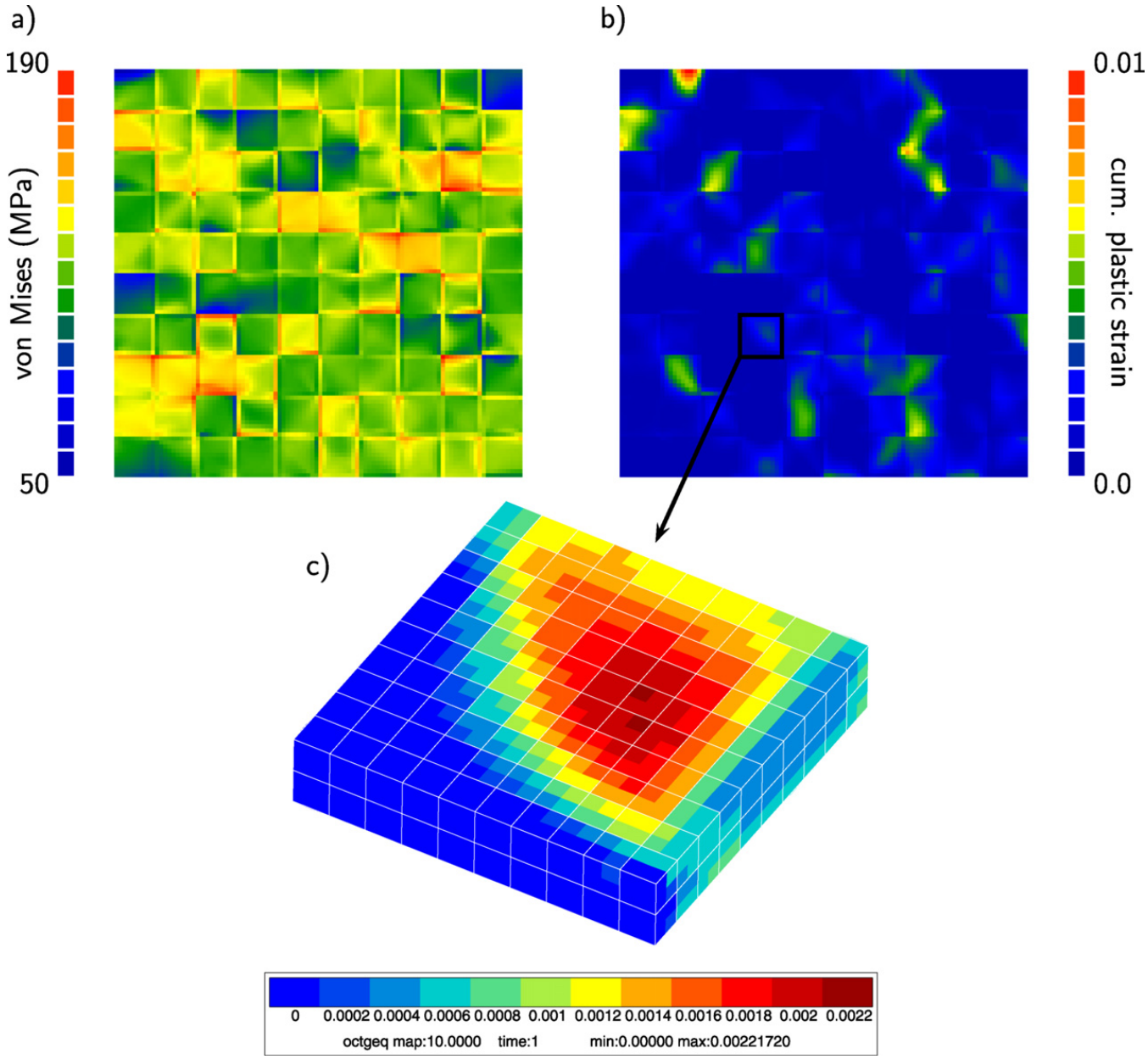

Fig. 7. Results of elastoplastic computations viewed from the top surface of the sample after applying 0.2% uniaxial tension; (a) von Mises equivalent stress, (b) plastic strain cumulated on all slip systems, (c) closeup on grain #64 (scale bar has been adjusted).

Fig. 7. Résultats des calculs en élastoplasticité à la surface de l'échantillon après 0,2% de traction moyenne : (a) contrainte équivalente de von Mises, (b) déformation plastique cumulée sur tous les systèmes de glissement, (c) détail du grain #64.

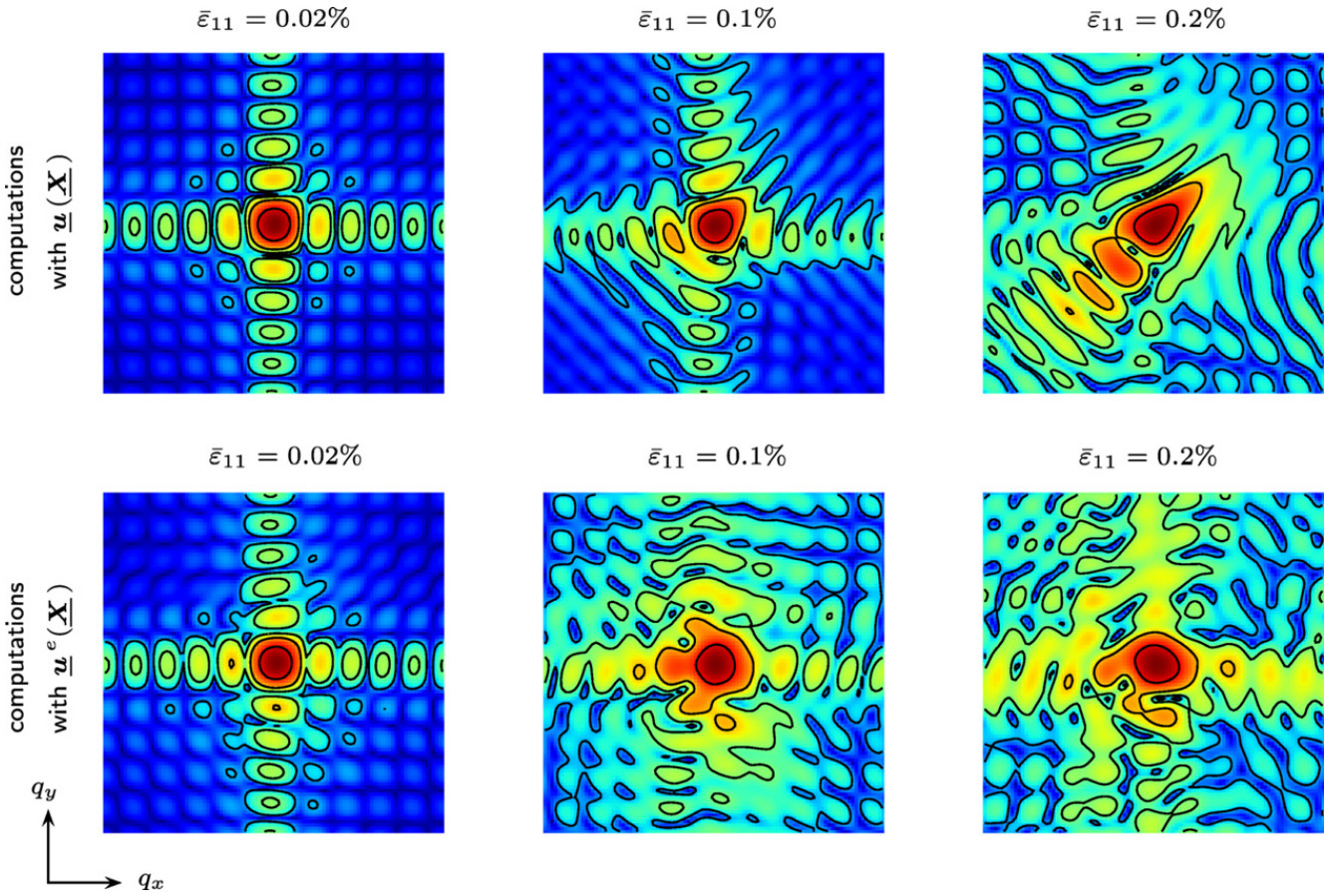

Fig. 8. Comparison of normalised CXD pattern predicted (corresponding to $q_z = 0$) in a polycrystalline sample mechanically loaded under 0.2% of axial strain using either the approximated field $\underline{\mathbf{u}}^e_{approx}(\underline{\mathbf{X}})$ or the full displacement field $\underline{\mathbf{u}}(\underline{\mathbf{X}})$; contour values are [0.3, 0.5, 0.7, 0.9].

Fig. 8. Comparaison entre les figures de diffraction cohérentes calculées (correspondant à $q_z = 0$) dans un échantillon polycristallin chargé à 0,2% de traction uniaxiale moyenne, obtenues en utilisant le champ de déplacement approché $\underline{\mathbf{u}}^e_{approx}(\underline{\mathbf{X}})$ ou le champ de déplacement total $\underline{\mathbf{u}}(\underline{\mathbf{X}})$; l'échelle des isovaleurs est [0,3, 0,5, 0,7, 0,9].

5. Total vs. elastic distortion effects in plastically deformed polycrystals

To evaluate the predicted CXD patterns when plastic deformation occurred, it is proposed to use the approximate displacement field defined in Eq. (22) instead of using the full displacement field. For that purpose, an ideal polycrystal has been computed using the crystal plasticity framework described in Section 3.1. The sample of dimensions $10 \times 10 \times 0.2$ µm^3, is composed by 100 square grains with a random orientation (see Fig. 6). The specimen is loaded under pure tension with a level of 0.2% total axial strain, typical of what might be observed in the experiments and sufficient to develop some plastic activity. The critical resolved shear stress for octahedral slip systems was taken as $\tau_c = 50$ MPa and no hardening was considered.

Elastoplastic computation results after mechanical loading are presented in Fig. 7. As expected, the mechanical straining produces more heterogeneities than what was observed previously with thermal loading.

CXD patterns have been computed for selected grains using either the approximated field $\underline{\mathbf{u}}^e_{approx}(\underline{\mathbf{X}})$ or the full displacement field $\underline{\mathbf{u}}(\underline{\mathbf{X}})$. A comparison is made in Fig. 8. One can see that after the onset of plasticity, the diffraction patterns are more distorted using $\underline{\mathbf{u}}(\underline{\mathbf{X}})$ than $\underline{\mathbf{u}}^e_{approx}(\underline{\mathbf{X}})$. Indeed, at this point the displacement field is no longer representative of the elastic stretch and rotation of the crystal lattice. In particular, the typical cross obtained from the square shape of the grains remains visible when using $\underline{\mathbf{u}}^e_{approx}(\underline{\mathbf{X}})$. From this point of view, the use of an approximate elastic field such as $\underline{\mathbf{u}}^e_{approx}(\underline{\mathbf{X}})$ proposed in the paper is needed to compare simulated CXD patterns to experimental ones.

6. Conclusion

This article presented a novel computational approach to help analyse coherent diffraction patterns. Currently a large research effort is dedicated to develop inversion techniques to retrieve elastic strains field and grain shapes using the patterns recorded from the illumination of a polycrystal sample (see Section 2). The present approach aims at a direct comparison of experimental and simulated CXD patterns. It is complementary of the usual inversion technique in the sense that it can be used to investigate the influence on diffraction patterns of parameters such as the grain shape, orientation, global texture, strain level, etc. As long as the sample deforms elastically, the full displacement field is used to simulate

CXD patterns but when plasticity starts to be activated, this is no longer true. We proposed to use an approximate elastic displacement field capturing the elastic rotation and stretch as opposed to the full displacement field. It was supposed here that each material volume element contains enough dislocations so that continuum mechanics can be applied.

Currently, coherent diffraction patterns have been obtained experimentally mainly for elastic cases. In the future, experiments will be carried out in the elastoplastic regime. The present work compared two ways of predicting such patterns, based either on the full strain field or only on the elastic deformation, the latter being probably more physically sound. This kind of approach may therefore be needed to interpret experimental diffraction patterns when the specimen experiences plastic strain. In the case of very low plastic activity, this simulation framework should be replaced by a discrete dislocation model which could supply the elastic displacement field around dislocations within the selected grain.

References

[1] G. Cailletaud, S. Forest, D. Jeulin, F. Feyel, I. Galliet, V. Mounoury, S. Quilici, Some elements of microstructural mechanics, Computational Materials Science 27 (3) (2003) 351–374.

[2] R. Brenner, R.A. Lebensohn, O. Castelnau, Elastic anisotropy and yield surface estimates of polycrystals, International Journal of Solids and Structures 46 (2009) 3018–3026.

[3] E. Héripré, M. Dexet, J. Crépin, L. Gélébart, A. Roos, M. Bornert, D. Caldemaison, Coupling between experimental measurements and polycrystal finite element calculations for micromechanical study of metallic materials, International Journal of Plasticity 23 (9) (2007) 1512–1539.

[4] A. Zeghadi, F. N'Guyen, S. Forest, A.-F. Gourgues, O. Bouaziz, Ensemble averaging stress-strain fields in polycrystalline aggregates with a constrained surface microstructure—Part 1: Anisotropic elastic behaviour, Philosophical Magazine 87 (8–9) (2007) 1401–1424.

[5] A. Zeghadi, S. Forest, A.-F. Gourgues, O. Bouaziz, Ensemble averaging stress-strain fields in polycrystalline aggregates with a constrained surface microstructure—Part 2: Crystal plasticity, Philosophical Magazine 87 (8–9) (2007) 1425–1446.

[6] L. St-Pierre, E. Héripré, M. Dexet, J. Crépin, G. Bertolino, N. Bilger, 3D simulations of microstructure and comparison with experimental microstructure coming from OIM analysis, International Journal of Plasticity 24 (2008) 1516–1532.

[7] W. Ludwig, A. King, P. Reischig, M. Herbig, E.M. Lauridsen, S. Schmidt, H. Proudhon, S. Forest, P. Cloetens, S. Rolland du Roscoat, J.Y. Buffière, T.J. Marrow, H.F. Poulsen, New opportunities for 3d materials science of polycrystalline materials at the micrometre lengthscale by combined use of X-ray diffraction and X-ray imaging, Materials Science and Engineering A 524 (1–2) (2009) 69–76 (Special topic section: Probing strains and dislocation gradients with diffraction).

[8] F. Eberl, S. Forest, T. Wroblewski, G. Cailletaud, J.-L. Lebrun, Finite element calculations of the lattice rotation field of a tensile loaded nickel base alloy multicrystal and comparison to topographical X-ray diffraction measurements, Metallurgical and Materials Transactions A 33 (2002) 2825–2833.

[9] D. Faurie, O. Castelnau, R. Brenner, P.O. Renault, E. Le Bourhis, P. Goudeau, In situ diffraction strain analysis of elastically deformed polycrystalline thin films, and micromechanical interpretation, Journal of Applied Crystallography 42 (2009) 1073–1084.

[10] N. Vaxelaire, H. Proudhon, S. Labat, C. Kirchlechner, J. Keckes, V. Jacques, S. Ravy, S. Forest, O. Thomas, Methodology for studying strain inhomogeneities in polycrystalline thin films during in situ thermal loading using coherent X-ray diffraction, New Journal of Physics 12 (3) (2010) 035018.

[11] F. Šiška, S. Forest, P. Gumbsch, Simulation of stress-strain heterogeneities in copper thin films: Texture and substrate effects, Computational Materials Science 39 (2007) 137–141.

[12] Filip Šiška, Samuel Forest, Peter Gumbsch, Daniel Weygand, Finite element simulations of the cyclic elastoplastic behaviour of copper thin films, Modelling and Simulation in Materials Science and Engineering 15 (1) (2007) S217–S238.

[13] F. Šiška, D. Weygand, S. Forest, P. Gumbsch, Comparison of mechanical behaviour of thin film simulated by discrete dislocation dynamics and continuum crystal plasticity, Computational Materials Science 45 (2009) 793–799.

[14] I.K. Robinson, C.A. Kenney-Benson, I.A. Vartanyants, Sources of decoherence in beamline optics, in: Proceedings of the Seventh International Conference on Surface X-ray and Neutron Scattering, Physica B: Condensed Matter 336 (1–2) (2003) 56–62.

[15] F. Livet, F. Bley, J. Mainville, R. Caudron, S.G.J. Mochrie, E. Geissler, G. Dolino, D. Abernathy, G. Grubel, M. Sutton, Using direct illumination CCDs as high-resolution area detectors for X-ray scattering, Nuclear Instrument & Methods in Physics Research A 451 (3) (2000) 569–609.

[16] J. Mandel, Une généralisation de la théorie de la plasticité de W.T. Koiter, Int. J. Solids Structures 1 (1965) 273–295.

[17] J. Mandel, Plasticité classique et viscoplasticité, CISM Courses and Lectures, vol. 97, Springer-Verlag, Udine/Berlin, 1971.

[18] J. Mandel, Equations constitutives et directeurs dans les milieux plastiques et viscoplastiques, Int. J. Solids Structures 9 (1973) 725–740.

[19] C. Teodosiu, F. Sidoroff, A theory of finite elastoviscoplasticity of single crystals, Int. J. of Engng. Science 14 (1976) 165–176.

[20] C. Teodosiu, Large Plastic Deformation of Crystalline Aggregates, CISM Courses and Lectures, vol. 376, Springer-Verlag, Udine/Berlin, 1997.

[21] M. Fivel, S. Forest, Plasticité cristalline et transition d'échelle : cas du monocristal, Techniques de l'Ingénieur, M4016, 2004, 23 pp.

[22] S. Kruch, Homogenized and relocalized mechanical fields, Journal of Strain Analysis for Engineering Design 42 (2007) 215–226.

[23] J.R. Neighbours, G.A. Alers, Elastic constants of silver and gold, Phys. Rev. 111 (3) (1958) 707–712.